Nanoscale

Accepted Manuscript

This article can be cited before page numbers have been issued, to do this please use: S. Manavalan, J. Ganesamurthi, S. M. Chen, P. Veerakumar and K. Murugan, *Nanoscale*, 2020, DOI: 10.1039/C9NR09148C.

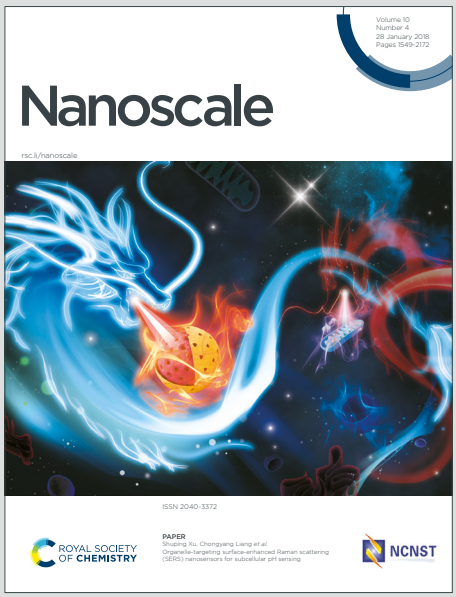

ROYAL SOCIETY OF CHEMISTRY

rsc.li/nanoscale

Nanoscale

View Article Online
DOI: 10.1039/C9NR09148C

ARTICLE

A robust Mn@FeNi-S/graphene oxide nanocomposite as a high efficiency catalyst for the non-enzymatic electrochemical detection of hydrogen peroxide†

Received 00th January 20xx,
Accepted 00th January 20xx

DOI: 10.1039/x0xx00000x

Shaktivel Manavalan,[a] Ganesamurthi Jaysiva,[a] Shen-Ming Chen,*[,a] Pitchaimani Veerakumar,[b,c] Murugan Keerthi[a]

Exploring high-efficiency, stable, and cost-effective electrocatalysts for electrochemical activities is greatly desirable and challenging. Herein, a newly designed hybrid catalyst with manganese-doped FeNi-S encapsulated into graphene oxide (Mn@FeNi-S/GO) with unprecedented electrocatalytic activity is developed by a simple one-step heating treatment and followed by sonication. X-ray powder diffraction (XRD), Raman spectroscopy, fourier transform infrared spectroscopy (FTIR), scanning electron microscope (SEM), high resolution transmission electron microscopy (HRTEM), X-ray photoelectron spectroscopy (XPS), and N_2 sorption isotherm demonstrates that successful formation of Mn@FeNi-S/GO. The electrochemical impedance spectroscopy (EIS) and cyclic voltammetry (CV) further confirm kinetic-favourable adsorption of hydrogen peroxide (H_2O_2) on surface sites of Mn@FeNi-S/GO. Additionally, the synergetic effects between Mn@FeNi-S and GO are regarded as significant contributors to an efficient electron transfer path and promote the capture of H_2O_2 in hybrid catalysts. Under an optimal biosensor-based Mn@FeNi-S/GO electrode exhibits a high sensitivity (8.929 $\mu A\ \mu M^{-1}\ cm^{-2}$) and a detection limit of 8.84 nM with a wide detection range for H_2O_2 and excellent selectivity, and is capable of online monitoring of H_2O_2 derived from apple juice and human blood serum.

1. Introduction

Hydrogen peroxide (H_2O_2) is a fundamental phenomenon in biological and chemical systems and plays a very important role in signal transduction of cells.[1,2] H_2O_2 as a prominent member of reactive oxygen species (ROS) serves as a global regulator of many physiological and pathological processes.[3-4] This regulation of the ROS level act as a valuable biomarker of various bodily disorders such as Alzheimer's disease, cancer, diabetes, oxidative stress, and neurodegeneration.[5,6] The capability of rapid and accurate H_2O_2 detection could be the ease of earlier diagnosis and clinical treatment of preventive and therapeutic strategies.[7,8] Furthermore, H_2O_2 as a versatile green oxidant, plays a vital role in chemical, pharmaceutical, environmental, food, and cosmetic industries.[9–11] However, the consumption of H_2O_2 could cause skin barrier functions and damage to the upper gastrointestinal tract.[12] Therefore, the development of an efficient sensor for H_2O_2 in chemical and biological environments is of urgency. In this regard, electrochemical technology has attracted much attention for online monitoring of H_2O_2 detection due to its simplicity, easy fabrication, low-cost, and high sensitivity.[13,14] However, traditional enzyme-based electrochemical detection of H_2O_2 suffers from a poor lifetime, which impedes its practical application. At present, plentiful efforts have been made for developing nanomaterial-based efficient non-enzymatic electrocatalysts for H_2O_2 detection, such as precious metals, transition metals, and carbon materials.

Up to date, a large variety of materials based on cost-effective transition metals and their derivatives such as metal

[a] Department of Chemical Engineering and Biotechnology, National Taipei University of Technology, Taipei 10608, Taiwan, ROC. E-mail: smchen78@ms15.hinet.net; Fax: +886-2-27025238
[b] Department of Chemistry, National Taiwan University, Taipei 10617, Taiwan, ROC
[c] Institute of Atomic and Molecular Sciences, Academia Sinica, Taipei 10617, Taiwan, ROC.

†Electronic Supplementary Information (ESI) available: Synthesis of GO, BET EDX, CV/i-t studies and Table S1. See DOI: 10.1039/x0xx00000x

View Article Online
DOI: 10.1039/C9NR09148C

chalcogenide,[15,16] metal phosphide,[17,18] metal nitride,[19,20] metal carbide,[21,22] and metal oxide or hydroxide,[23,24] have been developed for the electrocatalytic performance and have achieved impressive advancements. Among them, transition metal sulfides (TMSs) deserve particular attention owing to their natural abundance, low cost, and preferable catalytic activity.[25] In particular, first-row TMSs are a typical class of metalloid compounds with superior catalytic performance, which serves as a promising candidate for water splitting,[26] electrochemical sensors,[27] lithium storage,[28] and supercapacitor.[29] However, these materials suffer from poor cyclic stability, low electrical conductivity and deficient concentration of active sites that hinder their wide-range applications.[30] To overcome these issues, there have been many efforts to combine TMSs with suitable carbon materials such as the use of carbon nanotubes (CNTs), activated carbon, graphene and graphene derivatives. For instance, Liu *et al.*[31] prepared FeS NPs anchored on reduced graphene oxide nanosheets via direct-precipitation method for electrochemical sensor application. The synthesized FeS/rGO demonstrated outstanding electrocatalytic property towards simultaneous detection of biomolecules. Furthermore, Vu and co-workers[32] have reported reduced graphene oxide–nickel sulfide (NiS) composited on mechanical pencil lead by means of hydrothermal deposition. The fabricated MPL-NiS/rGO sensor was used to independently measure the toxic substances such as bisphenol-A (BPA) and mercury(II). which delivered outstanding electrochemical response for BPA and Hg^{2+} detection. Therefore, the rational design and synthesis of active, stable, and cost-effective catalysts are extremely favourable but remain the huge challenge for electrochemical sensor.

In this research, we focused on improving the catalytic efficiency of FeNi-S by doping Mn and combining active particles on the matrix of graphene oxide (GO) to improve electrochemical performance and stability significantly. Element doping, which is an effective method to change the surface electron structure of catalysts, has been reported to be beneficial for improving catalyst conductivity and developing additional active sites for electrochemical performance. However, the close contact between the Mn@FeNi-S particles and GO not only leads to a sequential conductive electron transfer network but also enables the encapsulating structure to further restrict the nanoparticles to a very small size, thus ensuring more active sites. The resulting hybrid Mn@FeNi-S/GO nanocomposite, therefore, showed remarkable catalytic performance for the reduction of H_2O_2 in neutral electrolytes and obtained strong good to excellent sensitivity with low detection limit. The synthesis process of the hybrid-like Mn@FeNi-S/GO nanocomposite, as shown in Scheme 1.

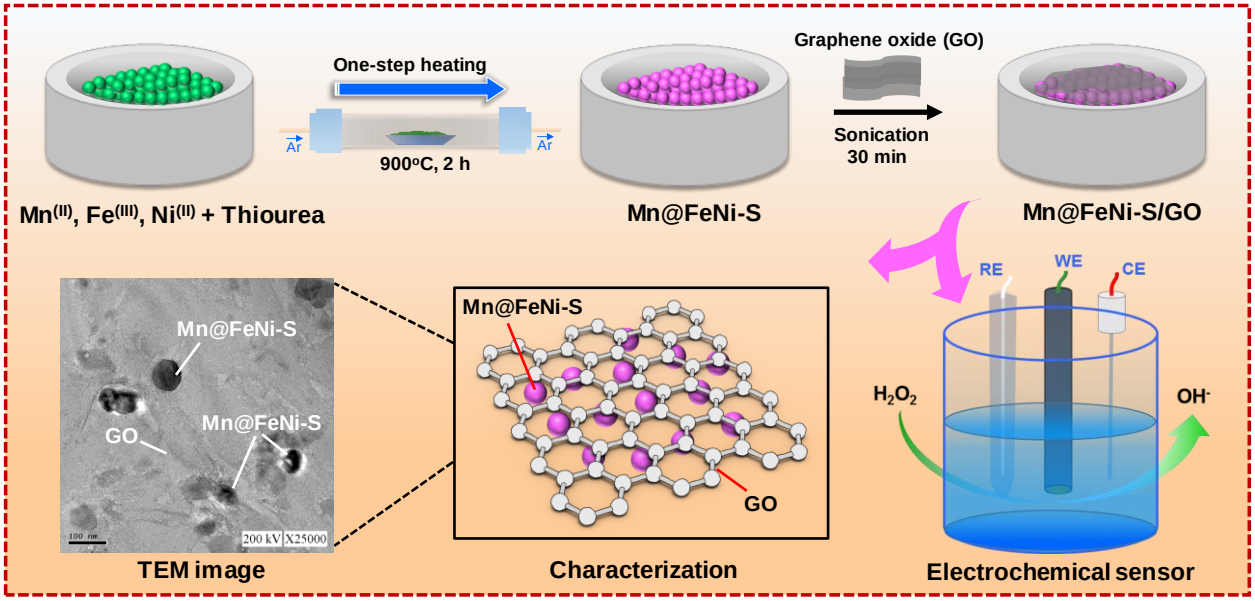

Scheme 1 Schematic diagram for the synthesis of Mn@FeNi-S/GO nanocomposite and its characterization and electrocatalytic performance.

2. Experimental

2.1. Chemicals

Graphite (powder, <20 μM, synthetic), iron(III) chloride hexahydrate ($FeCl_3$. $6H_2O$, 98%), nickel(II) chloride hexahydrate ($NiCl_2$. $6H_2O$, 99%), manganese(II) nitrate tetrahydrate ($Mn(NO_3)_2$. $4H_2O$, 97%), thiourea (CH_4N_2S, 99%), hydrogen peroxide (H_2O_2, 30% wt in H_2O, ACS reagent). and ethanol (C_2H_5OH, 99%), were brought from Sigma-Aldrich and used without further purification. The supporting electrolyte of phosphate buffer (PB, 0.1 M, pH 7.0) was prepared by using 0.1 M Na_2HPO_4 and NaH_2PO_4 solutions. The pH value of the solutions was adjusted with 0.5 M H_2SO_4 and 1.0 M NaOH. The water used throughout all experiments was purified through a Millipore system.

2.2. Real sample collections

Apple juice was purchased commercially from local mart and human blood serum sample was a 30 mL polypropylene syringe equipped with a silicone-coated stainless steel needle. This sample was transferred to a silicone-coated glass tube and centrifuged at 3000 rpm for 20 min. The supernatants were collected as the blood serum samples. Freeze-dried human blood serum reference material issued by the Chang Gung University (Research Institute) for Environmental studies was also used as a test sample in this preliminary study. ***Ethical statement:*** The research protocols of human blood serum was performed in compliance with the relevant laws and institutional guidelines for care and use of laboratory human subjects of Chang Gung University, Taiwan (R.O.C) in accordance with NIH Publication No. 00-4783 (2000). Consent was obtained from the human subject for experimentation and approved by the Affiliated Institutional Human Care and Use Ethics Committee of Chang Gung University, Taiwan (R.O.C).

2.3. Synthesis of Mn@FeNi-S/GO

Graphene oxide (GO) was synthesized from graphite powder by a simplified Hummer's method and detailed in the electronic supporting information (ESI†). In detail, 0.1 g of $FeCl_3{\cdot}6H_2O$ (0.370 mmol), 0.035 g of $NiCl_2{\cdot}6H_2O$ (0.27 mmol), 0.030 g of $Mn(NO_3)_2{\cdot}4H_2O$ (0.294 mmol), and 1.0 g of thiourea (13 mmol) were mixed homogenously by using mortar pestle. Subsequently, this mixture was placed on a porcelain boat and heated in a tube furnace at 900 °C for 2 h with a heating rate of 2 °C min^{-1} under argon atmosphere. Finally, the sample was allowed to natural cooling, the resultant powder was denoted as Mn@FeNi-S.

For the preparation of Mn@FeNi-S/GO nanocomposite, 100 mg of Mn@FeNi-S powder was dispersed in an ethanol solution (10 mL) followed by mixed with 100 mg of GO nanosheets under ultrasonic vibration at least for 30 min. During the ultrasonication process, the tiny Mn@FeNi-S particles are strongly immobilized on the GO nanosheets, due to the surface functional groups, which is labeled as Mn@FeNi-S/GO (see Scheme 1).

2.4. Characterizations

The field emission-scanning electron microscopy (FE-SEM) images were captured using the Hitachi S-3000 H microscope. The high resolution transmission electron microscopy (HRTEM) images were obtained using the Shimadzu JEM-1200 EX at an accelerating voltage of 200 kV. The elemental mapping and high-angle annular dark-field scanning transmission electron microscopy (HAADF-STEM) images were obtained using the Shimadzu JEM-1200 EX bonded with HORIBA EMAX X-ACT. The HRTEM images of GO were taken by JEOL JEM-2100F instrument operating at 200 kV. The XRD patterns were recorded on a XPERT-PRO spectrometer with Cu Kα radiation (λ = 1.54 Å). The Raman spectra were obtained using the NT-MDT, NTEGRA SPECTRA spectrometer. The fourier transform infrared spectroscopy (FTIR) results were obtained using Perkin-Elmer IR spectrometer. The XPS images were obtained using the Thermo ESCALAB 250 system. Nitrogen-sorption measurements were performed on a Micromeritics, ASAP 2020. All samples were degassed at 180 °C for 12 h prior to the actual measurement.

2.5. Electrochemical measurements

A conventional three-electrode system combined with a CHI-405a electrochemical workstation (CHI Instruments, USA) was used for the electrochemical measurements at room temperature (25 ˚C). A glassy carbon and rotating glassy carbon electrode (GCE, 0.07 cm^2 and RGC, 0.2 cm^2) coated with as-prepared nanocomposite, a platinum wire, and an Ag/AgCl electrode (with saturated KCl) were employed as the working, counter, and reference electrodes, respectively. The EIS spectra were measured by EIS, EIM6ex Zahner (Germany) with a frequency range of 100–0.01 Hz and amplitude of 5.0 mV at a constant overpotential of 150 mV in 0.5 mM $[Fe(CN)_6]^{3-/4-}$ containing 0.1 M KCl solution. The CV was performed in N_2-saturated 0.1 M phosphate buffer (pH 7.0) solution at a scan rate of 50 mV s^{-1} to obtain the polarization curves. Furthermore, the

amperometric response was measured at a constant overpotential of -0.25 V.

2.6. Fabrication of the electrodes

The catalyst suspensions (2.0 mg mL^{-1}) were prepared by dispersing 2.0 mg of the obtained catalysts into the 1.0 mL ultrapure water, followed by sonication for 1 h. On the other hand, GCE was polish/cleaned with alumina powder and rinsed in the ultrapure water flow. In the pre-treated GCE, 8.0 µL of prepared catalyst suspension was dropped on the electrode surface and air-dried. The loading amount of the catalyst was calculated to be 0.24 mg cm^{-2}.

3. Result and discussion

3.1. X-ray diffraction

The X-ray diffraction (XRD) patterns of GO, FeNi-S, Mn@FeNi-S, and Mn@FeNi-S/GO nanocomposite are presented in Fig. 1a. The characteristic peak at 10.2˚ was observed, which was corresponding to the (002) plane of GO.[33] The XRD peaks marked by the black triangles (Fig. 1a red line), the primary peaks located at 29.1˚, 31.2°, 35.6°, 45.7°, and 51.5° correspond to the (311), (222), (400), (511) and (440) facets of the face-centered cubic (*fcc*) FeNi-S (JCPDS card no. 75-0611) is presented, which indicated that FeNi-S was well crystallized.[34] Additionally, based on XRD database (#06-0696; Fe and #04-0850; Ni), iron and nickel are identified by the standard peaks (marked with "*") at 2θ of 65.02° and 82.33°, and 54.85° and 76.37° corresponding to (200) and (211), and (200) and (220), respectively, which indicates that some nanoparticles have a physical Fe/Ni mixture were detected.[35] The XRD lines for the Mn@FeNi-S and Mn@FeNi-S/GO nanocomposite samples also show that two additional lines (tiny peaks) evolve as extra planes, one at 2θ = 38.27° and the other at 2θ = 55.21°, corresponding, respectively, to the (400) and (440) planes of the Mn doping phase (marked with "♦"), which is consistent with those reported in the PDF for Mn (PDF 00-024-0508).[36] This observation indicates that the Mn@FeNi-S/GO nanocomposite have Ni, Fe, and Mn elements.

3.2. Raman analysis

Raman spectra for GO and Mn@FeNi-S/GO nanocomposite, as displayed in Fig. 1b exhibited the same features composed of two well-resolved broad bands, namely D (~1358 cm^{-1}), and G (~1594 cm^{-1}) band. Generally, D-band corresponding to A_{1g} symmetry mode which is associated with the disordered structures. It is formed from the sp^3-hybridized carbon atoms originating from defects and oxygen functional groups covalently bonded to graphenic structure. In contrast, the G-band is assigned to the E_{2g} symmetric center mode, arising from the sp^2-hybridized carbon atoms (C=C bonds) along the tangential direction of the hexagonal graphite lattice, characteristics of the ideal graphitization structure. Thus, the intensity ratio of D to G band (I_D/I_G) is indicative of the crystalline extent of the GO-based nanocomposites.

3.3. FTIR analysis

The FTIR spectra of GO, FeNi-S, Mn@FeNi-S, and Mn@FeNi-S/GO nanocomposite are shown in Fig. 1c. For pure GO, a broad band between 3400 and 3100 cm^{-1} is assigned to the **–**OH groups, whereas, the peak at 1737 cm^{-1} is the characteristic C=O stretching vibrations. In addition, the appearance of peak at 1401 cm^{-1} was ascribed to the C**–**OH stretching due to the presence of the hydroxyl and carboxyl groups bound to the basal planes and edges of GO sheets.[37] Obviously, a small peak was observed at 602 cm^{-1} in Mn@FeNi-S, which is attributed to the bending vibration of metal sulphide.[38] Moreover, a decrease peak intensity in the Mn@FeNi-S/GO nanocomposite confirms that the Mn@FeNi-S have successfully incorporated with GO nanosheets.

Nanoscale

View Article Online
DOI: 10.1039/C9NR09148C

ARTICLE

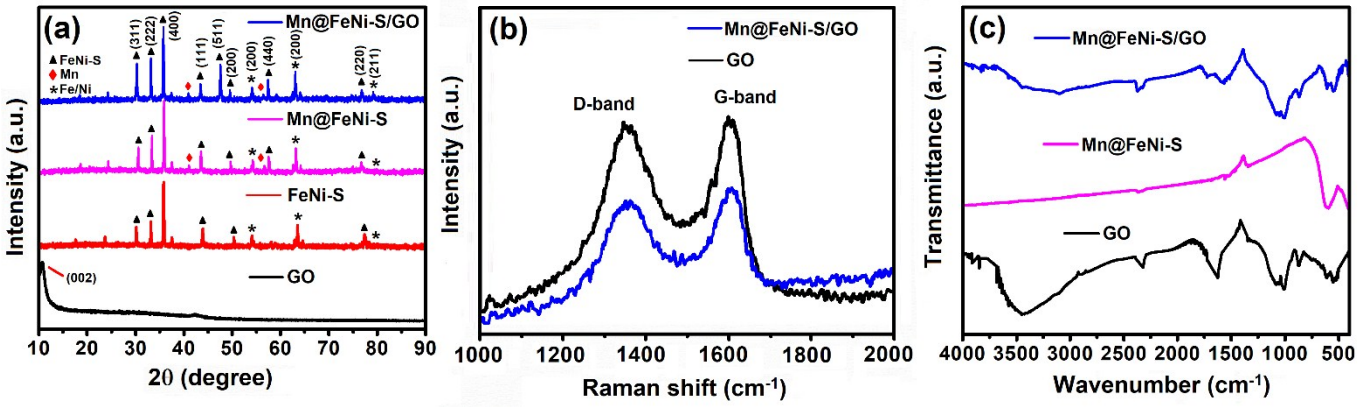

Fig. 1 (a) XRD patterns of GO, FeNi-S, Mn@FeNi-S, and Mn@FeNi-S/GO; (b) Raman spectra of GO and Mn@FeNi-S/GO, and (c) FTIR spectra of GO, Mn@FeNi-S, and Mn@FeNi-S/GO.

3.4. N_2 adsorption-desorption

The N_2 adsorption-desorption isotherms and the Brunauer–Emmett–Teller (BET) surface area values of GO and Mn@FeNi-S/GO nanocomposite were examined, as given in Fig. S1 (ESI†).The GO nanosheets having a bulk surface area of approximately 11.604 m^2 g^{-1}. The prepared Mn@FeNi-S/GO nanocomposite, the surface area is decreased because of the preferential blocking of the pores by the small size polycrystalline Mn@FeNi-S. It can be understood from the reduction in the mesopore volume of GO wherein the actual pore volume is decreased from 0.0065 cm^2 g^{-1} to 0.0042 cm^2 g^{-1}.

3.5. Structural properties

The nanostructured morphologies of GO, FeNi-S, Mn@FeNi-S, and Mn@FeNi-S/GO nanocomposite were investigated by FE-SEM, as shown in Fig. 2. Fig. 2a-d shows the GO consisted of folded and wrinkled sheets that were randomly aggregated in a disordered structure. This wrinkled aspect can be explained by the oxidation process to promote the admission of hydroxyl and epoxy functional groups. The morphologies and structure of Mn@FeNi-S nanoparticles are shown in Fig. 2e-h illustrates the highly aggregated of as-synthesized Mn@FeNi-S. Moreover, the Mn@FeNi-S nanoparticles are anchored on the GO surface and interconnected to form the three-dimensional porous architecture (see Fig. 2i-l). This result indicates that the Mn@FeNi-S nanoparticles have successfully fixed on the curled and thin wrinkled GO sheets.

Nanoscale

View Article Online
DOI: 10.1039/C9NR09148C

ARTICLE

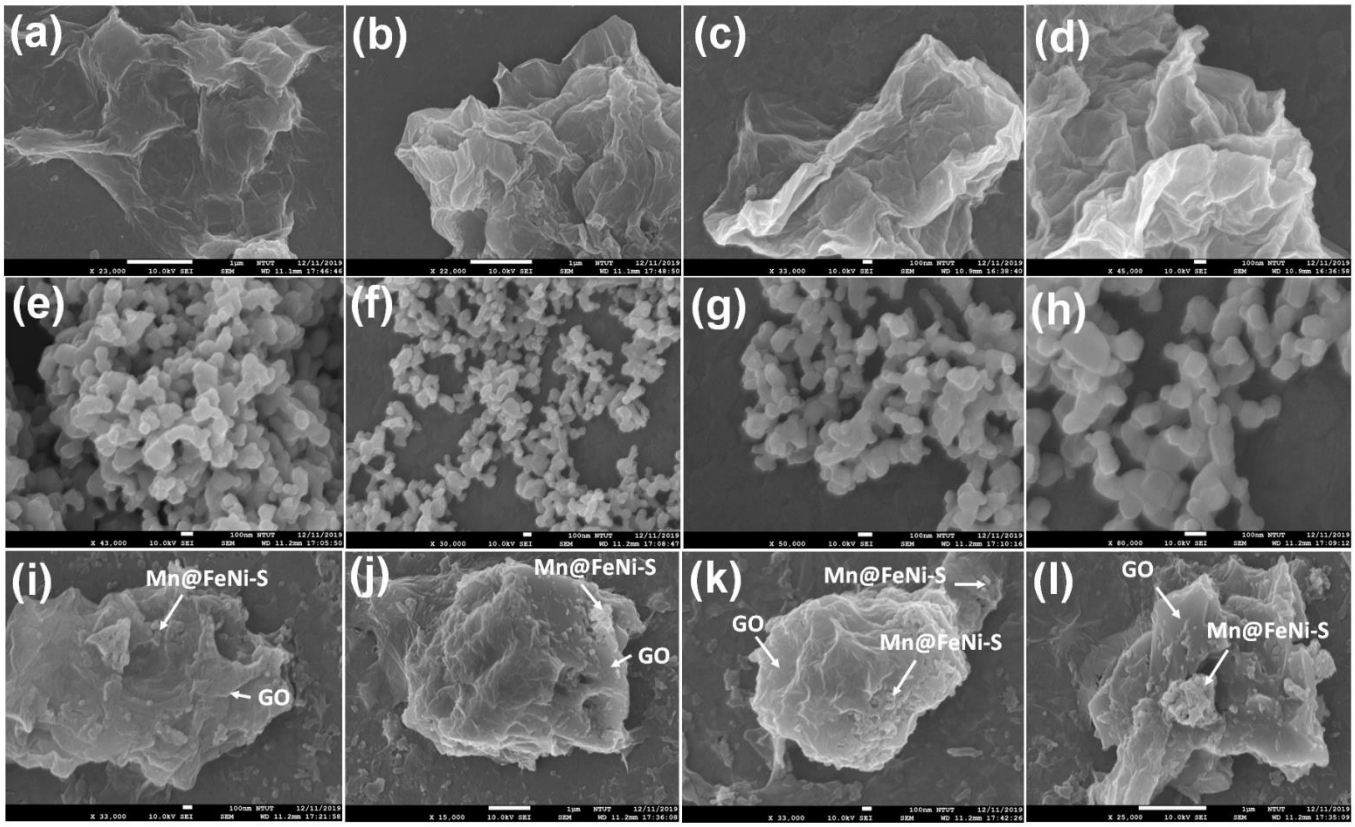

Fig. 2 Typical FE-SEM images of GO (a-d), Mn@FeNi-S particles (e-f), and Mn@FeNi-S/GO (i-l) nanocomposite.

The microstructure of the GO, Mn@FeNi-S particles, and Mn@FeNi-S/GO nanocomposite was further examined by HR-TEM (Fig. 3). Fig. 3a-d describes the TEM micrographs of the GO sheets morphology, with a wrinkled appearance with several folds, which may be due to a large number of functional groups, such as hydroxyl, carboxyl on the edge, and carboxyl and epoxide groups in the inner part. In addition, on higher magnification, a better image of the GO nanosheets emerged (Fig. 3d). A large number of Mn@FeNi-S sphere like secondary particles with a size of ca. 155 $\pm$ 20 nm are observed as well as certify the crystallinity, as shown in Fig. 3e-h. Besides, these Mn@FeNi-S particles are firmly attached to the GO nanosheets, strong sonication was applied during the preparation of HR-TEM specimens (see Fig. 3i-l), indicating that an excellent adhesion of the composites between GO nanosheets. A closer observation is made by TEM as shown in Fig. 3k, which provides further evidence that the Mn@FeNi-S particles are successfully anchored on the surface of GO sheets. A high-magnification TEM image (Fig. 3l) of composite reveals that lattice spacing of around 0.224 nm and 0.226 nm, corresponding to that of (200) and (111) of the crystal structure of the FeNi, respectively. Additional measurement (Inset Fig. 3l) by selected area diffraction (SEAD) confirm the crystalline structure of Mn@FeNi-S particles from the SEAD pattern based on the previous report.[37]

Nanoscale

View Article Online
DOI: 10.1039/C9NR09148C

ARTICLE

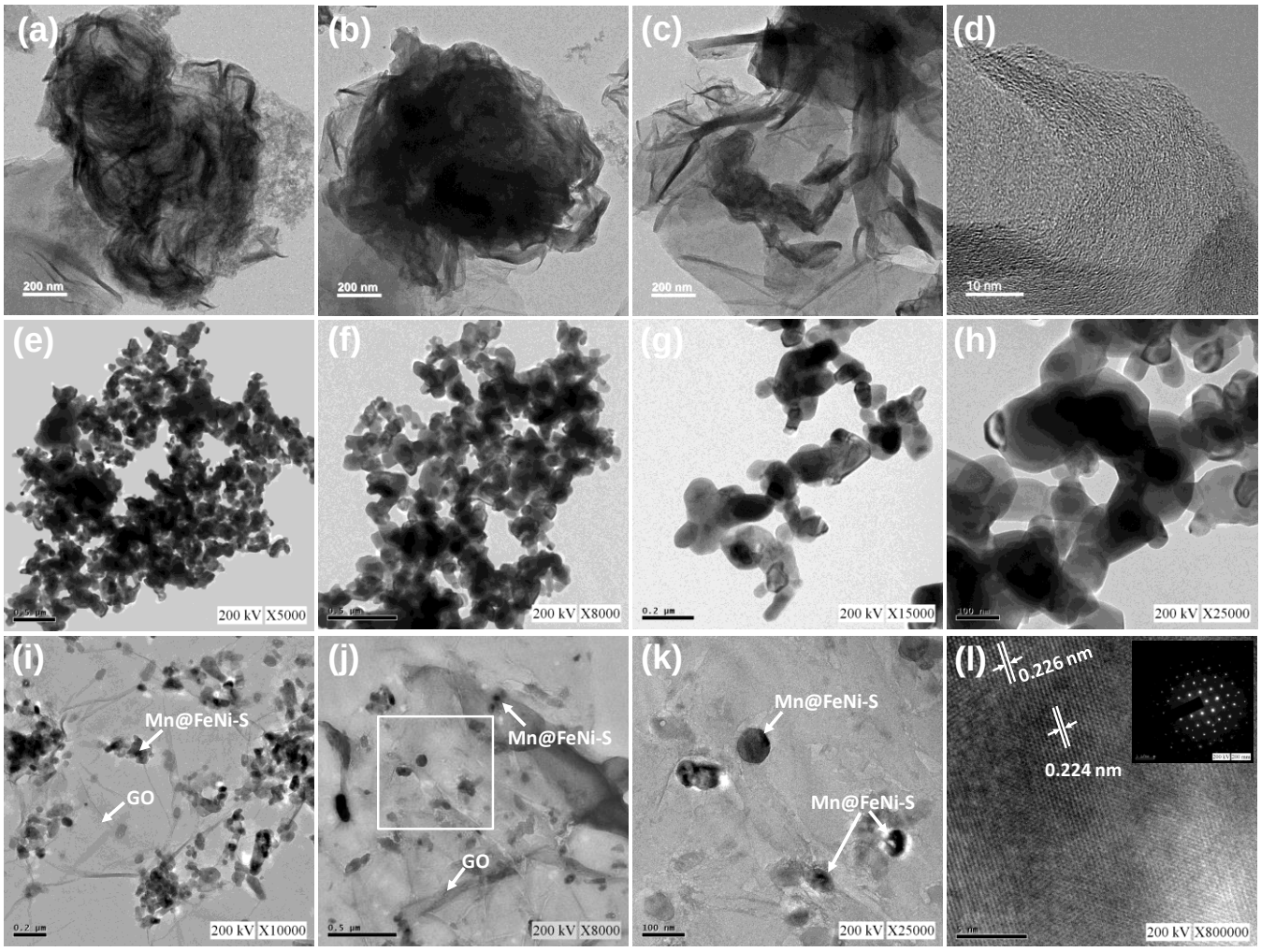

Fig. 3 Low- and high-magnification HR-TEM images of GO sheets (a-d), Mn@FeNi-S (e-h), and Mn@FeNi-S/GO (i-l) nanocomposite (Inset Fig 3l is corresponding SEAD pattern).

The elemental mapping images indicate the spatial distribution of the elements (Mn, Fe, Ni, and S) present in Mn@FeNi-S as shown in Fig. S2 (ESI†). It is observed that the density distribution of FeNi-S matches well with S; the coexistence of C, O and trace level of N confirm the loading of GO on the surface of Mn@FeNi-S (see Fig. S3, ESI†). All of the above results corroborate that Mn@FeNi-S/GO nanocomposite materials along with polycrystallized structure through the sonication synthesis technique were successfully prepared. The atomic percentage of various elements present in the nanocomposite is evaluated based on energy dispersive X-ray analysis (EDX) and shown in Fig. S3h (ESI†). We also performed to repeat the synthesis procedure to get the same stoichiometric composite, which is shown in Fig. S4 (ESI†). The high angle annular dark-field scanning transmission electron microscopy with energy-dispersive X-ray spectroscopy (HAADF-STEM-EDS) was employed to determine the elemental mapping of Mn@FeNi-S/GO nanocomposite as shown in Fig. S5 (ESI†). As a reference of this image and elemental mapping of an individual Mn@FeNi-S particle was uniformly distributed on the GO nanosheets support. Fig. S5a_1-a_6 (ESI†) display the elemental mapping image of C (yellow dots) and

View Article Online
DOI: 10.1039/C9NR09148C

O (blue dots) from GO matrix, whereas the Fe (green dots), Ni (red dots), Mn (orange dots) and S (magenta dots) clearly reveal that Fe, Ni, and Mn metals distributed homogenously, verifying the solid-solution nature present in the Mn@FeNi-S/GO nanocomposite. Additionally, the line scan results show that the abundant elements of the nanoparticle are C, O, S, Fe, Ni, and Mn (Fig.S5b_1-b_9) on the GO surface of the Mn@FeNi-S particle. These results further confirmed the successful incorporation of Mn@FeNi-S particle into the GO nanosheets.

3.6. X-ray photoelectron spectroscopy

To investigate the surface chemical compositions and valence states of the Mn@FeNi-S/GO nanocomposite by X-ray photoelectron spectroscopy (XPS) and the corresponding results were shown in Fig. 4a-g. As shown in Fig. 3a, the XPS scan survey spectra reveal the presence of S, C, O, Mn, Fe, and Ni elements. The higher-resolution XPS spectrum of S 2p region (Fig. 4b) shows two peaks of binding energy (BE) at 162.6 and 163.8 eV, which corresponded to S $2p_{1/2}$ and S $2p_{3/2}$ in FeNi-S, respectively. However, an additional peak located at 168.8 eV is assigned to the oxidized S species. The deconvoluted C 1s XPS spectrum of Mn@FeNi-S/GO is resolved into three components as displayed in Fig. 4c. The BE peaking at 285.5 eV originates from the C–C or C=C bond and the peaks at 287.3 and 289.6 eV are attributed to C–O/C–O–C and O–C=O bond, corresponding to alkoxy and carboxyl, respectively. In Fig. Fig. 4d, the O 1 s profile can be fitted to three BE peaks at 532.0, 534.1, and 536.6 eV, which can be attributed to the oxygen in C=O/C–OH, C–O, and O-C=O of the Mn@FeNi-S/GO nanocomposite, respectively. These results indicate the existence of the oxygen functional groups, such as alkoxy, carboxyl, or hydroxyl on the surface of GO and anchor Mn@FeNi-S to form an integrated nanocomposite. Specifically, the high-resolution XPS spectra of the Mn 2p (Fig. 4e), Fe 2p (Fig. 4f), Ni 2p (Fig. 4g), and regions of the catalyst are split into $2p_{3/2}$ and $2p_{1/2}$ doublets due to the spin-orbit coupling. The high resolution spectrum of Mn 2p exhibited two broad peaks at 642.9 and 654.9 eV corresponding to Mn $2p_{1/2}$ and Mn $2p_{3/2}$, respectively.

The binding energy of Mn $2p_{3/2}$ at 644.2 eV can be attributed to Mn^{3+}, and the effect of the high-valence Mn species is clear that the Mn^{3+} will aid in enhancing the catalytic activity. The Mn 2p region of the Mn@FeNi-S/GO nanocomposite exhibits no peak characteristic of MnS, thus suggesting that the formed catalyst is the Mn@FeNi-S/GO nanocomposite. The Fe $2p_{3/2}$ and $2p_{1/2}$ peaks are located BE at 711.6 and 725.4 eV, respectively, which can be assigned to the Fe in FeNi-S.[38] Similarly, the binding energy of the Ni 2p peaks is located at 857.2 and 874.3 eV, which corresponds to Ni $2p_{3/2}$ and Ni $2p_{1/2}$ in FeNi-S, respectively.[39]

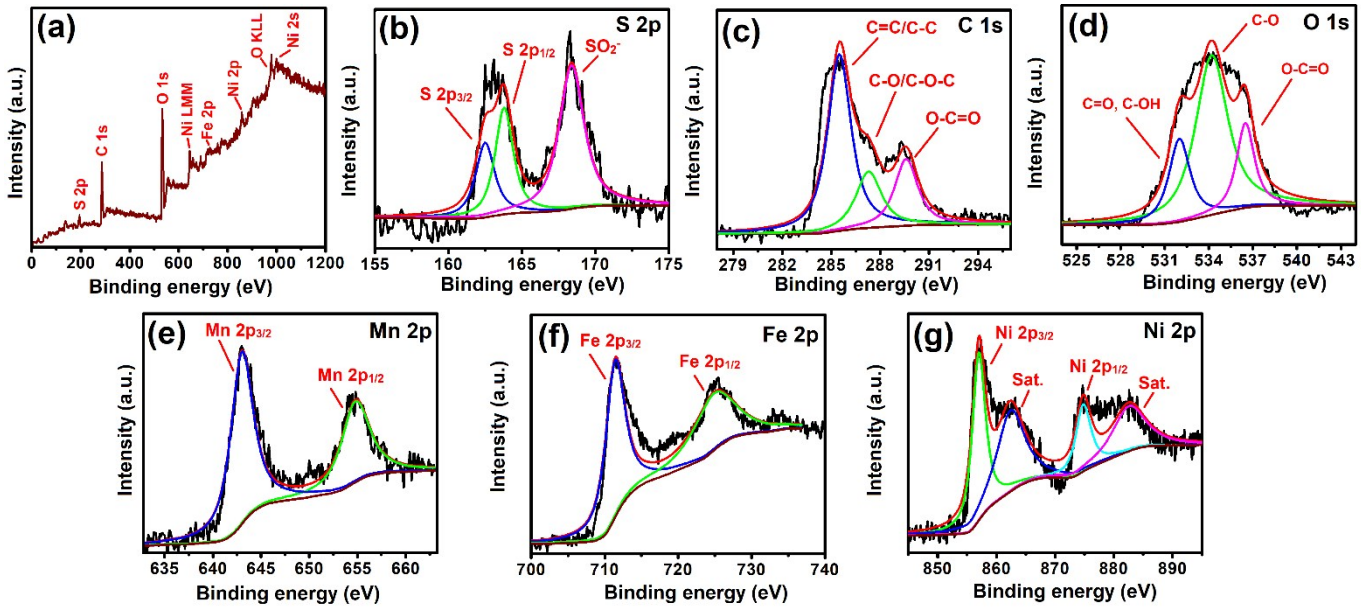

Fig. 4 (a) XPS survey spectra, (b) High resolution spectra of S 2p, (c) C 1s, (d) O 1s, (e) Mn 2p, (f) Fe 2p, and (g)Ni 2p region for Mn@FeNi-S/GO nanocomposite.

3.6. Electrocatalytic activity of Mn@FeNi-S/GO/GCE

To understand the conductivity of Mn@FeNi-S/GO nanocomposite in an electrode-electrolyte interface,

electrochemical impedance spectroscopy (EIS) was performed in 0.5 mM $[Fe(CN)_6]^{3-/4-}$ containing 0.1 M KCl. The EIS plots reveal that the Mn@FeNi-S/GO nanocomposite exhibits a smaller semicircle diameter than the Mn@FeNi-S, GO, and FeNi-S (Fig. 5a). The charge transfer resistance (R_{ct}) was also calculated by fitting the Randle's equivalent circuit model as depicted in Fig. 5a (inset). The R_{ct} of the Mn@FeNi-S/GO nanocomposite (57.0 Ω) is smaller than that of the Mn@FeNi-S (70.9 Ω), GO (330.8 Ω), and FeNi-S (458.1 Ω). This result indicates that GO incorporation can significantly reduce the impedance during electron transport and that Mn doping can also efficiently minimize the charge transfer resistance, thereby causing a favorable charge transfer resistance (R_{ct}) of the Mn@FeNi-S/GO nanocomposite in the ferricyanide system. Furthermore, the cyclic voltammetry (CV) was assessed to gain more insight into the Mn@FeNi-S/GO nanocomposite and shown in Fig. 5b. The electrochemical redox peak current (ERPC) of the Mn@FeNi-S/GO nanocomposite is higher than that of the Mn@FeNi-S, FeNi-S, and GO catalysts. The large ERPC of the Mn@FeNi-S/GO nanocomposite can be attributed to its large specific surface area and the increased number of active sites by doping; these properties reveal the excellent electrocatalytic activity of the Mn@FeNi-S/GO nanocomposite. The catalytic kinetics of Mn@FeNi-S/GO nanocomposite was also studied with different scan rates from 20 to 400 mV s^{-1}. As shown in Fig. 5c, the redox peak current of catalyst increased while scan rates increased from 20 to 400 mV s^{-1}, demonstrating the small polarization curve of the Mn@FeNi-S/GO/GCE in an aqueous electrolyte and the fast kinetics of the electrode. The linear plot of I_{pa} and I_{pc} peak current versus the square root of the scan rate is displayed in Fig. 5d with a coefficient (R^2) of 0.9958 and 0.9992, respectively.

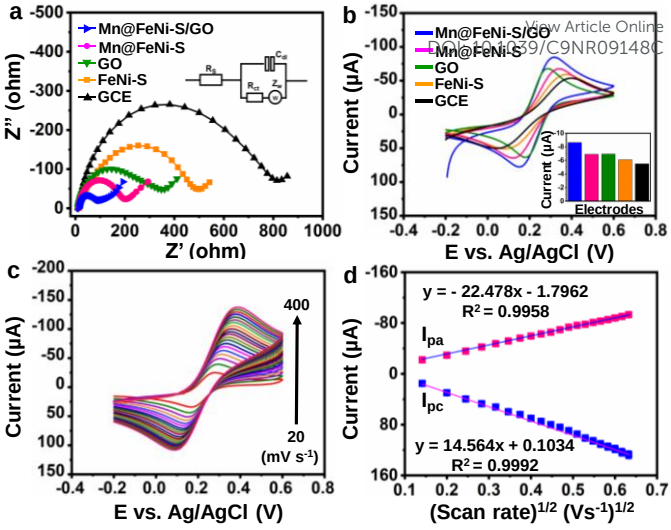

Fig. 5 (a) Nyquist plots of samples (Inset shows the corresponding equivalent circuit), (b) CV curves of bare GCE, GO, FeNi-S, Mn@FeNi-S, and Mn@FeNi-S/GO/GCE at scan rate of 50 mV s^{-1}, (c) CV curves of Mn@FeNi-S/GO-modified GCE at different scan rates range from 20–400 mV s^{-1}, and (d) The corresponding plot of peak current versus square root of scan rate. All experiments were conducted at 0.5 mM $[Fe(CN)_6]^{3-/4-}$ containing 0.1 M KCl.

3.6. Electrochemical behavior of Mn@FeNi-S/GO/GCE

The electrocatalytic activity of GO, FeNi-S and Mn@FeNi-S Mn@FeNi-S/GO GCEs for H_2O_2 (25 μM) was investigated by cyclic voltammetry (CV) in N_2-saturated 0.1 M PB (pH 7.0) at a scan rate of 50 mV s^{-1} (Fig. 6a). As expected, the Mn@FeNi-S/GO-modified GCE exhibits the highest electrocatalytic response toward H_2O_2 in contrast to the GO, FeNi-S and Mn@FeNi-S. The peak current of Mn@FeNi-S/GO/GCE for H_2O_2 reduction is remarkably greater than that of GO, FeNi-S, and Mn@FeNi-S/GO/GCE. This result reveals that the doping of the Mn element and the incorporation of GO can significantly improve the catalytic activity of FeNi-S. Additionally, the Mn-doping content is fundamental for the electrocatalytic activity of the FeNi-S catalyst. Consequently, we found that the electrocatalytic performance of FeS/GO, NiS/GO, and MnS/GO were studied in the same experimental condition (see Fig. S6, ESI†). It reveals that a slight current response for H_2O_2 (25 μM) while comparing to the Mn@FeNi-S and Mn@FeNi-S/GO modified GCEs. Based on these results, the most active Mn species is doped with the FeNi-S, which enhances the active site and increases the electrically conductive nature. Moreover, the synergetic effect also plays between Mn@FeNi-S active sites as well as GO functional groups further

View Article Online
DOI: 10.1039/C9NR09148C

promote the fast electrocatalytic response of H_2O_2.[42] Simultaneously, the CV response of Mn@FeNi-S/GO/GCE in with and without of H_2O_2 are presented in Fig. 6b. It can be seen that there is no reduction peak in the N_2-saturated 0.1 M PB (pH 7.0), demonstrating that the CV response of the Mn@FeNi-S/GO/GCE was entirely from H_2O_2 reduction. The reduction of H_2O_2 to two OH^- at the Mn@FeNi-S/GO electrode was electro catalyzed by Mn@FeNi-S/GO // Mn@FeNi-S/GO (OH) redox, according to the FeNi-S/GO // Mn@FeNi-S/GO(OH) redox, to the following reactions:

$$\boldsymbol{Mn@FeNi-S/GO + H_2O_2 \leftrightarrow Mn@FeNi-S/GO.H_2O_2} \quad (\mathbf{1})$$

$$\boldsymbol{Mn@FeNi-S/GO.H_2O_2 + e^- \rightarrow Mn@FeNi-S/GO.(OH) + OH^-} \quad (\mathbf{2})$$

$$\boldsymbol{Mn@FeNi-S/GO.(OH) + e^- \leftrightarrow Mn@FeNi-S/GO + OH^-} \quad (\mathbf{3})$$

$$\boldsymbol{H_2O_2 + 2e^- \rightarrow 2OH^- (Final\ Product)} \quad (\mathbf{4})$$

Based on this discussion and the previous reports,[40,41] it can be concluded that the electroreduction of H_2O_2 rate was totally controlled by two limitations, including, the adsorption process and the electron transfer rate. Thus, the catalyst with enhanced absorption properties and excellent electron transfer performance would be favored for H_2O_2 reduction. A couple of reasons for the brilliant performance of the catalyst as follows. At first, heteroatom S doping into the Mn@FeNi and with GO could induce an effective positive charge enhancement and highly distributions of the molecular orbital delocalization which leads to the weakening of O−O bond in H_2O_2. Thus, the additional benefits for enhancing of H_2O_2 adsorption. Second, based on the Nyquist impedance measurements, Mn@FeNi-S/GO nanocomposite showed low resistance, which guaranteed its fast electron transfer property. As a result, it proved that the Mn@FeNi-S/GO is the most active electrode for H_2O_2 reduction. Additionally, the CV curves of Mn@FeNi-S/GO/GCE in N_2-saturated 0.1 M PB (pH 7.0) containing various concentrations of H_2O_2 range from 25–125 µM at a scan rate of 50 mV s^{-1} are displayed in Fig. S7a (ESI†). The peak current intensity observed for H_2O_2 gradually increased as the concentration varied from 25–125 µM, indicating the rapid electron transfer rate of the Mn@FeNi-S/GO nanocomposite. The corresponding plot of peak current against the concentration of H_2O_2 exhibits linear with the regression equation of I_{pa} = -0.0684(μM) − 8.517 and the coefficient (R^2) of 0.9986, as shown in Fig. S7b (ESI†). These results revealed that the Mn@FeNi-S/GO nanocomposite possessed the good electrochemical sensing of H_2O_2 among the other composites.

3.7. Effects of catalyst dosage, pH and scan rate

The effect of Mn@FeNi-S/GO electrocatalyst loading on the electrode was performed with varied concentration such as 2, 4, 6, 8, and 10 mg mL^{-1} using CV in N_2-saturated 0.1 M PB (pH 7.0) containing H_2O_2 (50 µM) at a scan rate of 50 mV s^{-1}. As observed in Fig. S7c (ESI†), the peak current of H_2O_2 significantly increased as the concentration of catalyst increases from 2–6 mg mL^{-1}. Further, while increasing the concentration of catalyst from 6–10 mg mL^{-1}, as a result, the peak current was decreased, indicating that the electrode becomes saturated due to the mass dense thickness of the electrode surface. Notably, the 6.0 mg mL^{-1} of the catalyst modified electrode showed a higher peak current, therefore, it was chosen as an optimum concentration dosage of the electrode fabrication process.

To further explore the influence of different pH values on the electrochemical reduction of H_2O_2 at the Mn@FeNi-S/GO/GCE was assessed by CV in N_2-saturated different pH values ranging from pH (3.0–9.0, 0.1 M PB) at a scan rate of 50 mV s^{-1}. As can be seen in Fig. S7d (ESI†), the significant current response of H_2O_2 was noted at pH 7.0 than that at other pH values, owing to the higher electrocatalytic activity of Mn@FeNi-S/GO toward H_2O_2 detection (pH 7.0). The Mn@FeNi-S/GO also delivered catalase-like activity to H_2O_2 reduction at pH 7.0, indicating its ability to protect normal cells/tissues from oxidative stress. Hence, pH 7.0 has been considered as a supporting electrolyte in this study.

To better interpret the improved electrochemical performance of the Mn@FeNi-S/GO, the reaction kinetics was analyzed by CV at different scan rates from 20–300 mV s^{-1} in N_2-saturated 0.1 M PB (pH 7.0) containing 25 µM of H_2O_2. As depicted in Fig. 6c, the peak current intensity of H_2O_2 rapidly increased with the increase of scan rates from 20–300 mV s^{-1}, representing its exceptional electrocatalytic activity. Fig. 6d shows the linear plot between peak current of H_2O_2 and the square root of scan rates with a regression coefficient of y = -54.894x + 5.6294 (R^2 = 0.9965) and demonstrating the diffusion-controlled process has occurred. Furthermore, the reduction peak potential of H_2O_2 gradually shift towards the more negative potential as the scan rates increase from 20–300 mV s^{-1}, indicating that the fast electron transfer process. Obviously, an additional proper electronic confinement obtained from the doping of the Mn

View Article Online
DOI: 10.1039/C9NR09148C

element; also the abundant surface active provided by GO and FeNi-S were accelerating the charge and mass transfer. Thus, these features allow to more favorable electrocatalytic kinetics on the Mn@FeNi-S/GO catalyst for H_2O_2 reduction.

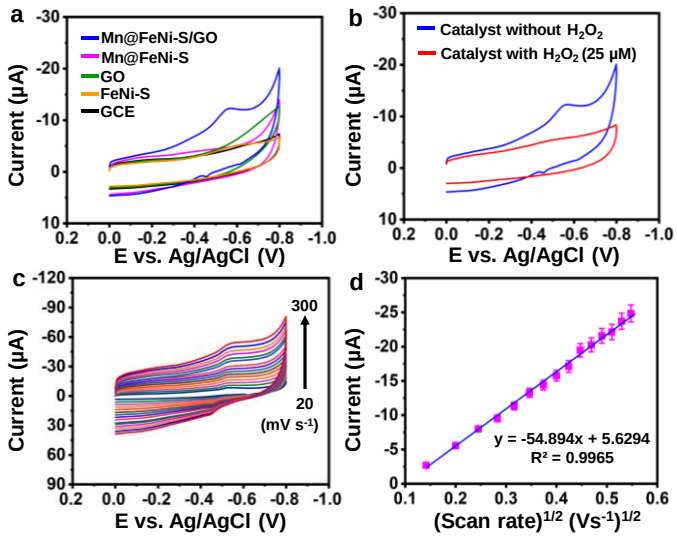

Fig. 6 (a) CV curves of bare GCE, GO, FeNi-S, Mn@FeNi-S, Mn@FeNi-S/GO-modified GCEs. containing 25 μM of H_2O_2 at a scan rate of 50 mV s^{-1}. (b) CV curves of Mn@FeNi-S/GO/GCE in with and without addition of 25 μM H_2O_2, (c) CV curves of Mn@FeNi-S/GO modified at different scan rates range from 20–300 mV s^{-1} in 25 μM of H_2O_2 and, (d) The corresponding plot of peak current versus square root of scan rate. All experiments were conducted in N_2-saturated in 0.1 M PB (pH 7.0).

3.8. Kinetic studies of Mn@FeNi-S/GO

In order to gain insight into the electrochemical kinetic rate of Mn@FeNi-S/GO nanocomposite was investigated by chronoamperometry (CA) in N_2-saturated 0.1 M PB (pH 7.0) at a potential of -0.68 V. Fig. 7a displays the CA response of the Mn@FeNi-S/GO/GCE in with and without the addition of H_2O_2. It was observed that a quite current response for the without addition of H_2O_2, which might originate from their surface defects. However, as 50 μM of H_2O_2 was successively injected in N_2-saturated 0.1 M PB (pH 7.0) at the Mn@FeNi-S/GO/GCE and as the result, the current response was increased greatly and was higher than that of bare. According to equation (5), the value of kinetic rate constant (K_{cat}) can be estimated.[42]

$$I_p/I_b = (\pi K_{cat} C_o)^{1/2} \qquad (5)$$

where I_p and I_b are the obtained current in with and without the addition of the H_2O_2, K is the catalytic rate constant, C_o is the substrate concentration (mol cm^{-3}) and t is the time (s). Considering Fig. 6a (inset), the K value of 1.61 × 10^4 M^{-1} s^{-1} may be derived from the relationship of I_c/I_L versus $t^{1/2}$. Further, the I_p increases as the concentration of H_2O_2 increased and shown in Fig. 7b. In addition, the diffusion coefficient (D) of H_2O_2 reduction may also be estimated by the Cottrell equation:

$$I_P = \frac{nFAC\sqrt{D}}{\sqrt{\pi t}} \qquad (6)$$

where I_p denotes the peak current (in A), n is the number of electron, F = 96,485 C mol^{-1} is the Faraday constant, A is the surface area of the electrode (cm^2), C represents bulk concentration of the analyte (mol cm^{-3}), and t is time (s). According to Fig. 7c, by taking the eq. 6, the value of D = 2.32 × 10^{-3} cm^2 s^{-1} for H_2O_2. Moreover, the surface coverage of the electroactive species (Γ) on the Mn@FeNi-S/GO-modified electrode may be calculated from the equation:[43]

$$I_P = \frac{n^2F^2A\Gamma v}{4RT} \qquad (7)$$

where υ is the scan rate (mV s^{-1}), R is the gas constant (8.314 J mol^{-1} K^{-1}) and T is the temperature (in ◦C). By using Fig. 6d and Eqn. 7, the Γ value was calculated to be 7.44 × 10^{-11} mol cm^{-2}. The above values of K, D, and Γ so obtained are in close agreements with those reported earlier for the other H_2O_2 sensors.[44] In addition, the plot of peak potential (E_p) showed a linear relationship over the log of scan rates. Based on the literature, the linear relationship can be expressed as the following as the Eqn.8 [45]

$$E_p = K + \left[\frac{2.303RT}{2\alpha n_\alpha F}\right]\log v \qquad (8)$$

where E_p is the peak potential of H_2O_2 reduction, α is the transfer coefficient for H_2O_2 reduction, $n\alpha$ is the electron transfer number involved in the rate-determining step of H_2O_2 reduction, K is a constant; R, T and, F have their usual significance. Assuming that one-electron transfer is the rate-determining step (n = 1), the values of α and n involved during the electron transfer process were calculated as 3.37 and 5.19, respectively.

The outstanding performance of the Mn@FeNi-S/GO sensor can be attributed to its excellent electronic transfer capability. One possible H_2O_2 reduction process is the two-electron reduction catalysis of H_2O_2 to H_2O. However, the one-electron reduced intermediate product OH ads (OH adsorbed on the catalyst) has strong oxidation capability, which is harmful to the catalyst. During the electrocatalysis process, the H_2O_2 molecules are chemisorbed on the sites of FeNi NPs moieties of Mn@FeNi-S/GO, and then directly reduced to H_2O without any intermediates through two-electron reduction process. This due to the quasi-four-electron transfer capability of metal-S/carbon electrocatalysts.[46]

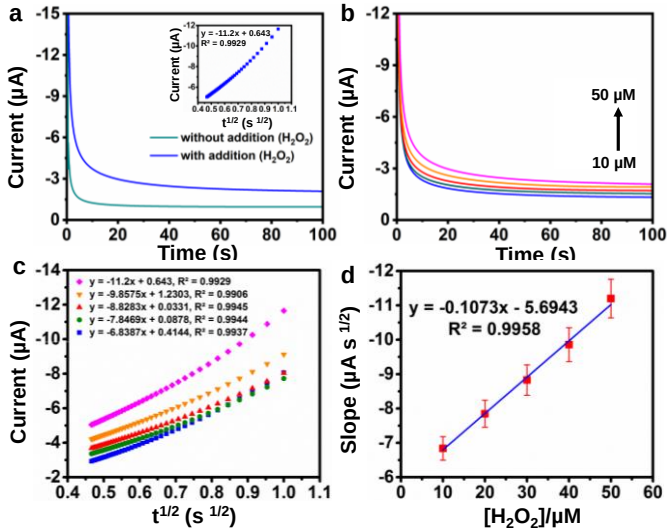

Fig. 7 (a) Chronoamperometric (CA) response of Mn@FeNi-S/GO/GCE in with (50 μM) and without addition of H_2O_2, (b) CA response of various concentration of H_2O_2 (10–50 μM) at the Mn@FeNi-S/GO, (c) The plot of current response versus square root of time, and (d) The representative plot of slope value versus H_2O_2 concentration.

3.9. Amperometric determination of H_2O_2

The amperometric (*i-t)* technology as rapid and high sensitive to detection of low concentration of H_2O_2 and it is a convenient tool for selectivity. Thus, further applied to evaluate the electrochemical performance of Mn@FeNi-S/GO towards H_2O_2 sensing. Fig. 8a shows the amperometric performance of the Mn@FeNi-S/GO with step by step successive injection of various concentrations of H_2O_2 into N_2-saturated 0.1 M PB (pH 7.0) at a potential of -0.25 V with electrode rotating speed of 1200 rpm. The Mn@FeNi-S/GO exhibited a rapid current response to a certain amount of H_2O_2 injection and reaches the steady-state within 4s, demonstrated the excellent electrocatalytic activity of Mn@FeNi-S/GO. As depicted in Fig. 8b, the current response of H_2O_2 was linearly changed with the concentration of H_2O_2 ranging from 0.055–523 μM and the obtained two linear regressions are expressed as $I_{\mu A}$ = -1.1875(μM) - 2.1401 (R^2 = 0.9915) and $I_{\mu A}$ = -0.3117(μM) - 3.9648 (R^2 = 0.9948). Based on these equations, the detection limit (LOD) can be estimated to be 8.84 nM using the standard formula LOD = 3(SD/slope) and the sensitivity was calculated to be 8.929 μA μM^{-1} cm^{-2}. In addition, the amperometric performance of Mn@FeNi-S was also assessed for H_2O_2 sensing and the obtained result was comparatively inferior to that of Mn@FeNi-S/GO electrode, as shown in Fig.S8 (ESI†). This is obvious that the electrochemical reduction of H_2O_2 was efficiently boosted by doping as well as synergetic effect also plays in the Mn@FeNi-S/GO nanocomposite. These analytical values (linear range, the limit of detection and sensitivity) were compared with the reported results from works of literature of heteroatom dopant, metal dopant, and ternary metal modified electrode for H_2O_2 sensor and summarized in Table S1 (ESI†). As evident, our proposed method had a wide linear range and a lower detection limit due to the excellent electrocatalytic activity of Mn@FeNi-S/GO to H_2O_2 reduction. Based on these results suggest that the Mn@FeNi-S/GO would be a promising electrochemical analytical tool for accurate and sensitive in online monitoring for H_2O_2.

3.10. Reproducibility, repeatability, and stability

The reproducibility of the electrode was evaluated by constructing five electrodes modified with Mn@FeNi-S/GO under a similar procedure and explored in N_2-saturated 0.1 M PB (pH 7.0) containing 25 μM of H_2O_2 by CV technique. The relative standard deviation (RSD) of the electrode's performance was ± 0.324 and indicates that this sensor had fantastic reproducibility. The repeatability of the sensor was examined by using a single electrode for five successive measurements of H_2O_2 (25 μM). The results reveal that the satisfying repeatability with RSD of ± 0.126, highlighting that this sensor exhibits good repeatability. The stability of a single electrode was also investigated by continuous measurement of H_2O_2 (25 μM) for 10 days. The electrode demonstrates impressive stability over 10 days' consecutive measurement, still retaining ≈ 97% of the initial response. The above results suggested that the Mn@FeNi-S/GO was appropriate for H_2O_2 detection in living systems, which may provide a robust method for further use in clinical purposes.

3.11. Interferents and real-time monitoring

To study the selectivity of Mn@FeNi-S/GO/GCE, amperometric measurements were performed by injecting the electroactive interferents of 0.1 M of (a) uric acid (UA), (b) L-ascorbic acid (L-AA), (c) dopamine (DA), (d) acetic acid (AA), (e) ethanol (ET), (f) L-Cysteine (L-Cys), (g) L-Leucine (L-Lun), (h) L-tyrosine (L-Try), (i) glucose (Glu), and (j) NaCl in N_2-saturated 0.1 M PB (pH 7.0) containing 10 μM H_2O_2. As presented in Fig. 8c, the presence of a 10-fold excess concentration of the above-mentioned interfering species with the target analyte causes insignificant current response changes of the H_2O_2 sensing system. This result evidently shows the excellent selectivity of the H_2O_2 over the Mn@FeNi-S/GO. Next, we carefully studied the practical use of Mn@FeNi-S/GO-based real-time monitoring of H_2O_2. Apple juice and human blood serum samples

were then chosen as a model. The recovery was evaluated by spiking H_2O_2 with three different concentrations (Fig. 8d). The synergistic effects for enhanced H_2O_2 adsorption in hybrid catalyst and performance of the sensor suggest a potential for exploring pathological and physiological roles of reactive oxygen species like H_2O_2 in biological environmental systems. Table 1 confirmed the recovery of 99.6 – 104.0 % for apple juice and 96.0 – 99.6 % for serum, which indicates that the H_2O_2 concentration was successfully relieved, likely owing to the rapid response and brilliant catalytic activities of Mn@FeNi-S/GO nanocomposite.

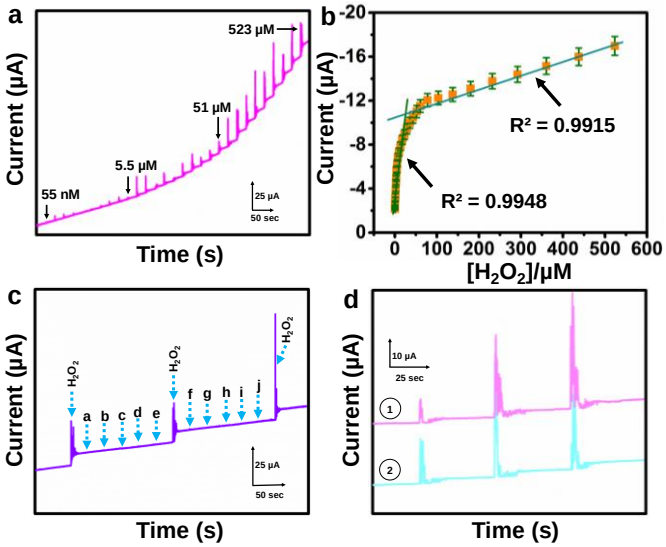

Fig. 8 (a) Amperometric *i-t* response of Mn@FeNi-S/GO nanocomposite in various successive addition of H_2O_2, (b) The corresponding plot of current response versus time (seconds), (c) The interferents studies of Mn@FeNi-S/GO in various interferents, and (d) The real-time monitoring of H_2O_2 in (1) apple juice and (2) human blood serum sample.

Table 1. Real-time detection of H_2O_2 in apple juice and human blood serum sample by *i-t.*

Real sample	Added [μM]	Detected [μM]	Recovery [%]	RSD* [%]
Apple juice	0.5	0.52	104.0	±1.3
	1.0	1.03	103.0	±1.8
	3.0	2.99	99.6	±2.1
Human blood serum	0.5	0.48	96.0	±2.4
	1.0	0.98	98.0	±3.5
	3.0	2.99	99.6	±2.2

*Measurement of three experiments (n=3).

4. Conclusions

In summary, we designed a new hybrid Mn@FeNi-S/GO nanocomposite via one-step heating treatment and subsequently by ultrasonication using $Mn^{(II)}$, $Fe^{(III)}$, $Ni^{(II)}$ salts, thiourea and GO, as precursors. The obtained Mn@FeNi-S/GO possesses high conductivity, nanostructure, and intimate contact between the Mn@FeNi-S and GO, thus resulting in high activity, fast mass/charge transport, easy release of formed electrons, and favorable stability for electrocatalytic processes. Consequently, when applied for electrochemical detection of H_2O_2, the Mn@FeNi-S/GO nanocomposite yields superior electrocatalytic activities in a neutral condition that possesses good sensitivity and has excellent potential for practical applications for H_2O_2 detection. This work provides a new strategy for the design and synthesis of highly active, stable, and novel structured transition metal derived catalyst for electrocatalysis applications.

Conflicts of interest

There are no conflicts to declare.

Acknowledgements

This work was supported by the Ministry of Science and Technology, Taiwan (MOST 107-2113-M-027-005-MY3).

Notes and references

1 J. Tang, Y. Quan, Y. Zhang, M. Jiang, A. M. Al-Enizi, B. Kong, T. An, W. Wang, L. Xia and X. Gong, *Nanoscale*, 2016, **8**, 5786–5792.
2 Y. Liu, X. Liu, Z. Guo, Z. Hu, Z. Xue and X. Lu, *Biosen. Bioelectron.*, 2017, **87**, 101–107.
3 B. D'Autréaux and M. B Toledano, *Nat. Rev. Mole. Cell Bio.*, 2007, **8,** 813.
4 N. Yusoff, P. Rameshkumar, M. S. Mehmood, A. Pandikumar, H. W. Lee and N. M. Huang, *Biosens. Bioelectron.*, 2017, **87,** 1020–1028.
5 D. Pramanik and S. G. Dey, *J. Am. Chem. Soc.*, 2010, **133**, 81–87.
6 Y. Wei, Y. Zhang, Z. Liu and M. Guo, *Chem. Comm.*, 2010, **46**, 4472–4474.
7 J. Xi, C. Xie, Y. Zhang, L. Wang, J. Xiao, X. Duan, J. Ren, F. Xiao and S. Wang, *ACS Appl. Mater. Inter.*, 2016, **8,** 22563–22573.
8 Y. Zhang, C. Wu, X. Zhou, X. Wu, Y. Yang, H. Wu, S. Guo and J. Zhang, *Nanoscale*, 2013, **5,** 1816–1819.
9 O. S. Keen, S. Baik, K. G. Linden, D. S. Aga and N. G. Love, *Environ. Sci. Techn.*, 2012, **46,** 6222–6227.

10 N. Akhtar, S. A. El-Safty, M. Khairy and W. A. El-Said, *Sens. Actuators B: Chem.*, 2015, **207,** 158–166.

11 W. Zhang, G. Fan, H. Yi, G. Jia, Z. Li, C. Yuan, Y. Bai and D. Fu, *Small*, 2018, **14,** 1703713.

12 M. Hara-Chikuma, H. Satooka, S. Watanabe, T. Honda, Y. Miyachi, Watanabe and T. A. Verkman, *Nat. Comm.*, 2015, **6,** 7454.

13 J. Xi, Y. Zhang, N. Wang, L. Wang, Z. Zhang, F. Xiao and S. Wang, *ACS App. Mater. Inter.*, 2015, **7,** 5583–5590.

14 J. Jia, B. Wang, A. Wu, G. Cheng and Z. Li, S. Dong, *Anal. Chem.*, 2002, **74,** 2217–2223.

15 S. Czioska, J. Wang, X. Teng and Z. Chen, *ACS Sustain. Chem. Eng.*, 2018, **6,** 11877–11883.

16 J.-X. Feng, J.-Q. Wu, Y.-X. Tong and G.-R. Li, *J. Am. Chem. Soc.*, 2018, **140,** 610–617.

17 B. Zhang, Y. Lui, H. H. Ni and S. Hu, *Nano Energy*, 2017, **38,** 553–560.

18 L. Yan, L. Cao, P. Dai, X. Gu, D. Liu, L.Li, Y. Wang and X. Zhao, *Adv. Funct. Mater.*, 2017, **27,** 1703455.

19 A. Wu, Y. Xie, H. Ma, C. Tian, Y. Gu, H. Yan, X. Zhang, G. Yang and H. Fu, *Nano Energy*, 2018, **44,** 353–363.

20 Z. Liu, H. Tan, J. Xin, J. Duan, X. Su, P. Hao, J. Xie, J. Zhan, J. Zhang and J.-J. Wang, *ACS Appl. Mater. Inter.*, 2018, **10,** 3699–3706.

21 L. Ai, J. Su, M. Wang and J. Jiang, *ACS Sustain. Chem. Engin.*, 2018, **6,** 9912–9920.

22 J.-X. Wu, C.-T. He, G.-R. Li and J.-P. Zhang, *J. Mater. Chem. A*, 2018, **6,** 19176–19181.

23 H. Cao, X. Zhou, C. Zheng and Z. Liu, ACS *Appl. Mater. Inter.*, 2015, **7,** 11984–11990.

24 W. Zhao, C. Zhang, F. Geng, S. Zhuo and B. Zhang, *ACS Nano*, *2014*, **8,** 10909–10919.

25 L. Jin, B.Liu, Y. Wu, S. Thanneeru and J. He, *ACS Appl. Mater. Inter.*, 2017, **9,** 36837–36848.

26 Q. Zhang, C. Ye, X. L. Li, Y. H. Deng, B. X. Tao, W. Xiao, L. J. Li, N. B. Li and H. Q. Luo, *ACS Appl. Mater. Inter*, 2018, **10,** 27723–27733.

27 Y. Dong, J. Li and L. Zhang, *Sens. Actuators B: Chem.*, 2019, 127208.

28 Y. Wang, R. Wei, B. Zhang, H. Lv, D. Xu, Q. Hao and B. Liu, *ACS Appl. Energy Mater.*, 2019, **2,** 6158–6162.

29 W. Liu, H. Niu, J. Yang, K. Cheng, K. Ye, K. Zhu, G. Wang, D. Cao and J. Yan, *Chem. Mater.,* 2018, **30,** 1055–1068.

30 A. Iwase, S. Yoshino, T. Takayama, Y. H. Ng, R. Amal and A. Kudo, *J. Am. Chem. Soc.*, 2016, **138,** 10260–10264.

31 X. Liu, E. Shangguan, J. Li, S. Ning, L. Guo and Q. Li, *Mater. Sci. Engin. C*, 2017, **70**, 628-636.

32 T. D. Vu, P. K. Duy, H. T. Bui, S.-H. Han and H. Chung, *Sens. Actuators B: Chem.,* 2019, **281**, 320-325.

33 R. Krishna, E. Titus, O. Okhay, J. C. Gil, J. Ventura, E. V. Ramana, J. J. Gracio, *Int. J. Electrochem. Sci.*, 2014, **9,** 4054–4069.

34 J. Jiang, S. Lu, H. Gao, X. Zhang and H.-Q. Yu, *Nano Energy* 2016, **27,** 526–534

View Article Online
DOI: 10.1039/C9NR09148C

35 N. A. M. Barakat, A.G. El-Deen, Z. K. Ghouri and S. Al-Meer, *Sci. Rep.* 2018, **8,** 3757.

36 S. A. Ahmed, *Results Phys.* 2017, **7**, 604–610.

37 M. Yuan, C. Nan, Y. Yang, G. Sun, H. Li, and S. Ma, *ACS Omega*, 2017, **2,** 4269–4277.

38 Z. Liu, H. Yu, B. Dong, X. Yu and L. Feng, *Nanoscale*, 2018, **10**, 16911–16918.

39 B. Zhang, C. Xiao, S. Xie, J. Liang, X. Chen and Y. Tang, *Chem. Mater.*, 2016, **28,** 6934–6941.

40 T. Zhang, Y. Gu, C. Li, X. Yan, N. Lu, H. Liu, Z. Zhang and H. Zhang, *ACS Appl. Mater. Inter.*, 2017, **9,** 37991–37999.

41 N. Lu, T. Zhang, X. Yan, Y. Gu, H. Liu, Z. Xu, H. Xu, X. Li, Z. Zhang and M. Yang, *Nanoscale*, 2018, **10,** 14923–14930.

42 C. Rajkumar, B. Thirumalraj, S.-M. Chen, P. Veerakumar and S.-B. Liu, *ACS Appl. Mater. Inter.*, 2017, **9,** 31794–31805.

43 E. Laviron, *J. Electroanal. Chem. Inter. Electrochem.*, 1974, **52**, 355–393.

44 H. Khoshro, H. R. Zare and R. Vafazadeh, *Chin. J. Catal.*, 2014, **35,** 247–254.

45 W. M. Costa, A. L. Marques, E. P. Marques, C. W.Bezerra, E. R. Sousa, W. S. Cardoso, C. Song and J. Zhang, *J. Appl. Electrochem.*, 2010, **40,** 375–382.

46 Z. Li, R. Liu, C. Tang, Z. Wang, X. Chen, Y. Jiang, C. Wang, Y. Yuan, W. Wang and D. Wang, *Small*, 2019, 1902860.

View Article Online
DOI: 10.1039/C9NR09148C

Table of content (TOC)

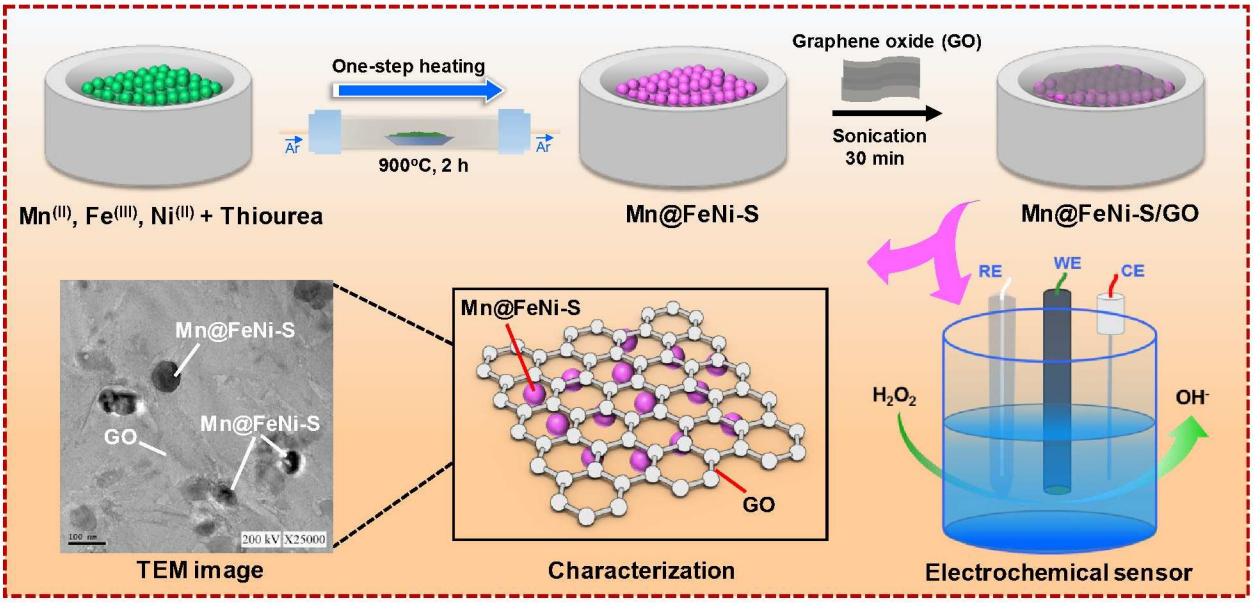

The synthesis procedure of Mn@FeNi-S/GO nanocomposite and its characterization and electrocatalytic performance